

# Designing Printed Circuit Stators for Brushless Permanent Magnet Motors<sup>1</sup>

*D. Gambetta and A. Ahfock*

## **Abstract**

Progress in a number of areas of technology has made printed circuit motors a serious contender for many applications. Modern cost effective neodymium magnets have allowed compact motor designs. Multi-layer circuit board production techniques have made the production of printed circuit coils cheaper and easier. However, in spite of the growing importance of printed circuit brushless motors, there is a lack of analytical tools to assist with their design. This paper uses geometrical analysis to allow the plotting of printed circuit tracks to be carried out more systematically. The track plotting procedures have been linked with the finite element method to predict rotational EMF waveforms. Six prototype motors were built and they were used to experimentally validate the method of predicting EMF waveforms. A general design algorithm is presented based on the suggested track plotting procedure and the EMF prediction technique.

**Keywords:** Printed Circuit Motors; Brushless Motors

## **1. Introduction**

The first printed circuit board motors, proposed more than four decades ago, were brushed DC motors [1, 2]. Progress in power electronics and the availability of low cost permanent magnets have led to the development of brushless printed circuit motors. These motors have some unique advantages such as high efficiency, zero cogging torque [3, 4] and reduced acoustic noise [5]. They allow design flexibility and are relatively

---

<sup>1</sup> This paper is a postprint of a paper submitted to and accepted for publication in IET Electric Power Applications and is subject to Institution of Engineering and Technology Copyright. The copy of record is available at IET Digital Library. Doi: 10.1049/iet-epa.2008.0199

easy to manufacture. For example a change in dimensions of a printed circuit stator can be accommodated without any major alterations to production equipment and processes.

Printed circuit motors are relatively small axial field motors and they are used in applications such as computer hard disk drives [3, 4]. Printed spiral coils are particularly suited to motors of such low dimensions. Some designers have adopted spirals with rhomboidal turns to avoid crowding at the inner radius of the substrate [3]. Others have aimed to fill the available substrate area completely and have adopted spirals with active sections running parallel with each other [6]. There is very little published work on justification for the use of particular coil geometries. In this paper, detailed analysis of the spirally shaped printed circuit coil is presented. The aim is to provide the printed circuit motor designer with a tool that will help maximize torque output for given motor dimensions.

Three coil shapes are considered. These are spirals with purely radial active sections, spirals with active sections running parallel with each other and spirals with each active section having a radial part and a parallel part. Throughout the paper, the term 'parallel' used in relation to track sections means parallel with the radial line that separates two adjacent coils. Equations are derived relating the number of turns ( $N$ ), the substrate inner radius ( $R_i$ ), the substrate outer radius ( $R_o$ ), the track width ( $w$ ) and the clearance between tracks ( $c$ ). To produce the printed stators, the tracks are plotted with the help of algorithms that maximizes the effectiveness of the coil. Theoretical predictions of EMF constants and EMF waveforms are presented in section 3 of the paper. The predictions are based on realistic flux distributions obtained from finite element analysis. Extensive tests on six prototype motors were carried out to validate the theory on which the proposed design techniques are based. A comparison between theoretical predictions and test results are presented in section 4. A general design algorithm based on the track plotting procedure and the EMF prediction technique is presented in section 5.

## 2. Analysis of Coil Geometries

Consider a section of the substrate as shown in figure 1. The simplest coil is made up of a spiral pair located on neighboring layers. The spirals are joined by a via located at their common centre. As shown in figure 1, current enters the coil from a terminal on the outer radius side of the substrate. It flows inwards, towards the coil center, through the tracks of one of the spirals, continues through the via at the centre of the spiral and then flows outwards, away from the coil center, through the tracks of the second spiral.

In general each turn of a coil may be considered to be made up of four sections. Two of those are non-active arc-shaped end-sections, one on the outer radius side and one on the inner radius side. The other two sections are active. The length of some of the arc-shaped inner end-sections may degenerate to zero for low values of  $R_i/R_o$ . To maximize the effectiveness of a coil with a given track width, its number of turns, average active length per turn and overall pitch factor must be maximized. The maximum EMF per unit length is obtained if the active conductor runs along a radial line. However, the number of turns can be severely affected if  $R_i/R_o$  is small and the active sections are constrained to be radial. For this reason purely radial coils are not given any further consideration. Parallel active sections are preferable although this leads to longer inactive sections. Coils with active sections which are partly parallel and partly radial are investigated because they offer the possibility of reduced total conductor length while maintaining performance in terms of EMF per unit speed or torque per unit current. Expressions are now derived for the maximum number of turns.

In figure 2 point X is at the centre of the coil and lies somewhere along the radial line which is the axis of symmetry of the coil. Proper placement of point X is required if a coil with maximum number of turns (N) is to be achieved. In general for given values of track width (w) and inter-track clearance (c), the number of turns is limited by  $(R_o - R_x)$  or  $XP$  or  $(R_x - R_i)$ . If X is placed too far towards the outer edge of the substrate, N is reduced

because it becomes restricted by the smaller value of  $(R_o - R_x)$ . Similarly, if X is placed too far towards the inner edge of the substrate, N is again reduced because it becomes restricted either by the smaller value of XP or by the smaller value of  $(R_x - R_i)$ . Based on the preceding arguments, it can be concluded that there is a position for X that results in the maximum number of turns. For small values of  $R_i/R_o$ , the number of turns is maximized if:

$$(R_o - R_x) = R_x \sin\left(\frac{\pi}{N_s}\right) \quad (1)$$

where  $N_s$  = number of spirals per layer

For larger values of  $R_i/R_o$ , the number of turns is maximized if:

$$(R_o - R_x) = (R_x - R_i) \quad (2)$$

From equation (1) it can be deduced that:

$$N = \frac{R_o \sin\left(\frac{\pi}{N_s}\right)}{(w+c) \left(1 + \sin\left(\frac{\pi}{N_s}\right)\right)} \quad (3)$$

Equation (3) is applicable if:

$$\left(\frac{R_i}{R_o}\right) \leq \frac{\left(1 - \sin\left(\frac{\pi}{N_s}\right)\right)}{\left(1 + \sin\left(\frac{\pi}{N_s}\right)\right)} \quad (4)$$

From equation (2) it can be deduced that:

$$N = \frac{(R_o - R_i)}{2(w+c)} \quad (5)$$

Equation (5) is valid if:

$$\left(\frac{R_i}{R_o}\right) \geq \frac{\left(1 - \sin\left(\frac{\pi}{N_s}\right)\right)}{\left(1 + \sin\left(\frac{\pi}{N_s}\right)\right)} \quad (6)$$

For a prescribed track width, equation (3) or (5) is to be used to determine N which has to be an integer. The equation can then be used again, with N fixed at its integer value, to readjust the track width to a higher value.

An example of a spiral coil with mixed track sections is shown in figure 3. Only the mid-track line is shown. A strategy has been adopted that maximizes the lengths of radial sections of the track subject to meeting minimum clearance requirements between tracks. This is achieved by keeping the track sections parallel on the inner radius side of arc XQ whose radius is defined by equation (1) or equation (2). Arc XQ is shown in figure 4. On the outer side of arc XQ, track sections are radial.

### 3. Predicting Coil EMFs

Back EMF per phase is an important measure of performance for a motor. The back EMF waveform allows deduction of the motor's torque capability and its torque quality. Prediction of back EMF waveforms requires knowledge of the flux density distribution. Depending on the level of accuracy required, this can be determined analytically or numerically. The machines being considered in this paper have relatively complex coil and magnetic circuit geometries and parts of the rotor iron may saturate magnetically. Consequently it is not possible to arrive at analytical expressions that will allow prediction of rotational EMF with better than ten per-cent accuracy. Therefore there is a need to rely on numerical methods. The adopted numerical techniques are presented in section 3.2.

In spite of its limited accuracy, an analytical technique can be valuable to those who have to shortlist design configurations that deserve detailed analysis. An equation is suggested in section 3.1 that can be used to evaluate the rotational EMF to a first approximation.

In both sections 3.1 and 3.2 it has been assumed that the number of rotor poles (P) is equal to the number of spirals ( $N_s$ ) per printed circuit layer. It is possible to construct three phase motors with  $N_s$  not equal to P, but such motors are not considered in this paper. Every stator under consideration was made up of three sets of printed layers circumferentially displaced from each other by 120 electrical degrees. An exploded view of one of the prototype motors is given in figure 5. All motors that were constructed are of the central stator dual rotor type.

### 3.1 Approximate Analytical Modeling

The major simplifying assumptions that had to be made to arrive at an analytical expression for rotational EMF are:

- (a) active track sections are in the radial directions and their lengths change linearly with angular position from ( $R_o - R_i$ ) at the coil's edge to zero at its centre;
- (b) the rotor iron has infinite permeability;
- (c) flux outside the rotor iron flows in the axial direction only;
- (d) flux density in the airgap is independent of radial and axial positions;

Equation (11) is based on the above assumptions.

$$E = \frac{\sqrt{2}NP(R_o + R_i)(R_o - R_i)B_{pk}\omega_m S_c}{2} \quad (7)$$

where:

E = EMF per spiral

$\omega_m$  = rotational speed

N = number of turns per spiral.

P = number of poles.

$$B_{pk} = \text{airgap peak flux density} = \frac{B_r t_m}{\left(t_m + \frac{g}{2}\right)}$$

$B_r$  = remanence of magnet.

$t_m$  = magnet thickness

$g$  = airgap length measured axially between opposite magnet surfaces

$S_c$  = combined length, spread and pitch factors of coil

$$= \frac{2}{\pi} \int_0^{\frac{\pi}{2}} \left(1 - \frac{2\theta}{\pi}\right) \cos \theta d\theta = \frac{4}{\pi^2}$$

$\theta$  = electrical angle

It has been assumed that the airgap flux density varies sinusoidally in the angular direction. This is a reasonable assumption because the effect of higher harmonics is significantly reduced as a result of the coils being distributed and short-pitched.

An approximate technique for determination of axial dimensions can be based on equations (8) and (9).

$$t_i = \text{axial thickness of rotor} = \frac{\pi B_{pk} S_m (R_o + R_i)}{2PB_s} \quad (8)$$

where:

$B_s$  = maximum allowable flux density in the rotor iron

$S_m$  = pitch factor magnet

$$t_a = \text{total axial length} = 2(t_i + t_g + t_m) + 3t_s \quad (9)$$

where:

$t_s$  = stator thickness per phase.

$t_g$  = clearance between magnet and stator surfaces

### 3.2 Predicting Coil EMFs Numerically

This section provides details of a numerical solution to the problem of predicting the phase EMF waveforms. For the purpose of determining motional induced EMF, the plane of the substrate is divided into cells as shown in figure 3. Each cell is bounded by a pair of radial reference lines and a pair of angular reference lines. The total EMF corresponding to a given rotor position is generally made up of contributions coming from each cell. The number of active track segments within a cell may be zero, one or two. Contributions to the total EMF are separately calculated for each segment by using equation (10).

$$dE = B^* \omega_m r dr \quad (10)$$

where:

$dE$  = contribution to total EMF from each track segment

$B^*$  = estimated flux density at point C in figure 6

$r$  = radial distance as shown in figure 6

$dr$  =  $(r_o - r_i)$  as shown in figure 6

$\omega_m$  = rotational speed

The estimated value ( $B^*$ ) of flux density is obtained by using:

$$B^* = B_1 w_o w_l + B_2 w_o w_r + B_3 w_i w_r + B_4 w_i w_l \quad (11)$$

where:

$$w_o = \frac{(r - r_s)}{(r_l - r_s)}$$

$$w_i = \frac{(r_l - r)}{(r_l - r_s)}$$

$$w_l = \frac{\theta_b}{(\theta_a + \theta_b)}$$

$$w_r = \frac{\theta_a}{(\theta_a + \theta_b)}$$

It is assumed that the flux density at the four corners of every cell ( $B_1$ - $B_4$  in figure 6) is known. In general flux density ( $B$ ) is a function of all spatial coordinates. Variation in the axial direction does not have to be considered since, for the purpose of coil EMF evaluation, it is reasonable to assume that all track segments making up a coil are at the same axial position. Flux distributions were obtained from finite element analysis.

As shown in figure 7, finite element modeling was carried out using FEMLAB®. Motors from 4 to 12 poles with dual rotor and central stator construction were considered. Existence of axial and circumferential symmetry meant that only half a pole pitch of one rotor had to be modeled. Figure 7 shows the model for a four pole motor. A plane of symmetry exists at  $z = 32.7$  mm. The axial flux density distribution on that plane is used to evaluate the EMF of the middle phase. There is no need for explicit modeling of the stator since all the materials making up the stator are assumed to have relative permeability equal to one and no stator current flows. In addition to the air subdomain whose relative permeability is taken to be one, there are three other subdomains that have been considered. These are the permanent magnet subdomain which in figure 7 is between  $z = 26$  mm and  $z = 30$  mm, the rotor back-iron subdomain which is between  $z = 22$  mm and  $z = 26$  mm and the sub-domain representing the non-magnetic shaft. Based on the manufacturer's data, a value of  $1.01e6$  H/m was used for the magnetization of the NdFeB permanent magnet. The rotor back-iron has been characterized by its magnetization curve which was determined experimentally by measurement carried out on material samples. The relative permeability of the shaft was taken as one. A typical axial flux density distribution obtained from finite element results is shown in figure 8.

As the rotor moves the flux distribution shown in figure 8 rotates relative to the radial reference lines shown in figure 3. As part of the algorithm that determines the rotational EMF waveform, the rotor position is changed in incremental steps and for each step a phase EMF value is calculated based on equation (10). A set of EMF values corresponding to one electrical cycle represents an EMF waveform. EMF waveforms for different phases are calculated using axial flux densities at the axial location of that phase.

#### **4. Experimental Verifications**

Six motors were built to validate the coil design and EMF prediction procedures that have been proposed. Details of the motors are given in table 1. All motors have an outer radius of 25 mm, a rotor iron thickness of 4 mm, a magnet thickness of 4mm, a nominal track width of 1 mm and a track clearance of 0.3 mm.

##### **4.1 EMF Waveforms**

A set of EMF waveforms for one of the prototype motors is shown in figure 9. For all six test motors, there is very good agreement between the predicted and measured waveforms. RMS values of the waveforms are given in table 1. The sine wave approximation for the EMF waveform is well-justified since the total harmonic distortion is less than 2%.

As expected, the EMF waveform of the middle phase within the stator stack has slightly lower magnitude than the outer phases. The difference is typically less than 3.5% and does not represent any significant problem to motor performance. EMF predictions by the first order model in section 3.1 are within ten percent of those based on finite element.

## 4.2 Thermal Considerations

Both from the point of view of stator temperature rise and from the point of view of efficiency a reduction of printed circuit coil resistance is desirable. However a reduction in phase resistance should not be at the expense of an excessive reduction in EMF. An objective assessment of different strategies to reduce phase resistance may be based on the value of  $\left(\frac{E}{\omega_m}\right)\sqrt{\frac{P_l}{R}}$  where  $P_l$  is the allowable stator power loss per phase. The term  $\left(\frac{E}{\omega_m}\right)\sqrt{\frac{P_l}{R}}$  is proportional to the torque capability of the motor. The constant of proportionality depends on the shape of the phase current which would be sinusoidal for synchronous motor mode of operation or quasi-square for brushless DC mode of operation. Comparison of the torque capabilities of different motors using the single term  $\left(\frac{E}{\omega_m}\right)\sqrt{\frac{P_l}{R}}$  is justified if armature reaction is neglected. Since the motors being considered have ironless stators, armature reaction is negligible. In the case of the prototype motors peak flux density due to rated stator current was less than 5 mT compared to the peak airgap flux density which was typically more than 0.5 T.

Allowable stator power loss can be estimated by thermal modeling or stator temperature rise test or both. For the prototype motors it was found by both thermal modeling and by test that, to keep substrate temperature rise below the acceptable level of 65°C,  $P_l$  has to be kept below 2.3 W. From the thermal investigations it was found that the temperature difference between the middle substrate and the exposed stator surface was less than 8°C. Table 1 provides  $\left(\frac{E}{\omega_m}\right)\sqrt{\frac{P_l}{R}}$  values for the six prototype motors, with  $P_l$  assumed to be 2.3 W.

There are a number of opportunities to reduce phase resistance. The use of mixed track is one which is covered in section 4.3 and illustrated in table 1. Another opportunity, which is not apparent in table 1, arises because the number of turns ( $N$ ) when calculated using the equations in section 2 is usually not an integer. The actual number of turns adopted is the next lower integer. Some substrate area is left and, as suggested in section 2.1, can be reallocated to increase track width to reduce resistance. This area could be substantial when  $N$  is low and in such cases phase resistance reduction could be very significant.

### **4.3 Parallel Track Sections versus Mixed Track Sections**

As shown in table 1 and in figure 10 the main advantage of coils with mixed track sections is lower phase resistance without substantially sacrificing the magnitude of rotational EMF. As expected, of the motors being considered, the four pole motors benefit the most from coils with mixed track sections because they have the highest effective curvature and therefore the highest ratio of non-active to active conductor length.

Table 1 also shows that the coils with fully parallel track sections have the higher EMF compared to coils with mixed sections. Parallel track sections have lower skew factors compared to radial track sections which have a skew factor of 1. But the coils with parallel sections have better pitch factors which more than compensate for the effect of their lower skew factors.

### **4.4 Number of Poles**

Predictions and test results shown in table 1 and in figure 10 suggest that benefits of higher EMF and lower phase resistance are possible if the number of poles is carefully chosen. There are two major factors affecting the magnitude of the phase EMF. These

are the magnitude of the air-gap flux density and the total number of turns. Since the circumferential gap between magnets, measured in electrical degrees, was kept the same irrespective of the number of poles, there is increased leakage between neighbouring magnets as the number of poles goes up. The consequence, as can be seen in table 1, is a decrease in the axial component of air-gap flux density with higher pole numbers. The number of turns and the skew factor both go up with number of poles. The combination of those factors results in the existence of an optimal value for the number of poles. As shown in figure 10, in the case of the prototype motors being considered, the optimum number of poles is eight.

## **5. Design Optimisation**

The experimentally validated EMF evaluation method and the suggested track plotting procedure can form the basis for a design optimization algorithm for printed circuit motors. In the example that follows, the design objective would be to maximize torque output capability subject to a number of constraints which are listed in Table 2.

The torque developed by the printed circuit motor is proportional to the product of the airgap flux density and the stator current. At one extreme, if the entire available axial length was allocated to the field system, torque will be zero because there would be no room left for the stator and stator current will be zero. The other extreme would be if the entire available axial length was allocated to the stator, excitation would be zero and again torque production would be zero because the field flux density would be zero. As the axial length allocated to the magnet and rotor iron is increased from zero, the output torque will rise to a maximum and then fall and reaches zero again when no room is left for the stator. The aim of the algorithm is to find this maximum.

For a given maximum stator power loss  $P_1$ , a lower phase resistance, achievable with a higher value of  $t_s$ , signifies a higher allowable stator current. Magnet axial thickness  $t_m$  and phase resistance  $R$  may be considered to be independent variables under the control of the designer. Design optimization means identifying the  $(t_m, R)$  pair that results in highest torque capability.

A design requirement is for the back EMF per unit speed to be within tight limits. Thus the number of turns per phase, is relatively constant. In a multilayer PCB design the total number of turns per phase, assuming all spirals are series connected, is  $N \times L$  where  $N$  is the number of turns in a spiral and  $L$  is the number of layers. For a given copper foil, different  $(N, L)$  pairs satisfy the EMF requirement. For every given value of  $t_m$ , a sub-optimum is found which would correspond to the  $(N, L)$  pair that results in the highest output torque. In cases where there is more than enough axial space to meet the EMF requirement, the algorithm automatically increases the number of layers. The coils on the additional layers are connected in parallel with the other coils. By paralleling the additional coils as uniformly as possible to the other coils overall phase resistance is minimized.

The algorithm consists of the following steps:

- (a) Set  $t_m$  equal to its minimum allowable value.
- (b) Make an initial estimate for  $t_i$  by simultaneous solution of equations (9) and (10).
- (c) Use finite element analysis to obtain the flux density distribution and, if necessary, repeat the FEM analysis with  $t_i$  re-adjusted until the peak flux density in the rotor iron is close to  $B_s$ .
- (d) Use equation (9) to calculate  $t_s$ .
- (e) For the copper foil being considered, calculate the maximum value of  $N$  using equation (3) or (5).

- (f) For each integer value of N between 1 and its maximum value, calculate if the constraints in Table 2 allow,  $\left(\frac{E}{\omega_m}\right)\sqrt{\frac{P_l}{R}}$ .
- (g) Select and plot against the current  $t_m$  the highest value of  $\left(\frac{E}{\omega_m}\right)\sqrt{\frac{P_l}{R}}$  from the current set of values obtained from step (f).
- (h) Increment  $t_m$  and go to step (b) if the maximum allowable value of  $t_m$  is not exceeded.
- (i) Repeat steps (a) to (h) for all candidate copper foil thicknesses
- (j) Read the graph from step (g) to obtain the maximum torque capability.

The graphical output from step (g) is shown in figure 11.

## **6. Conclusions**

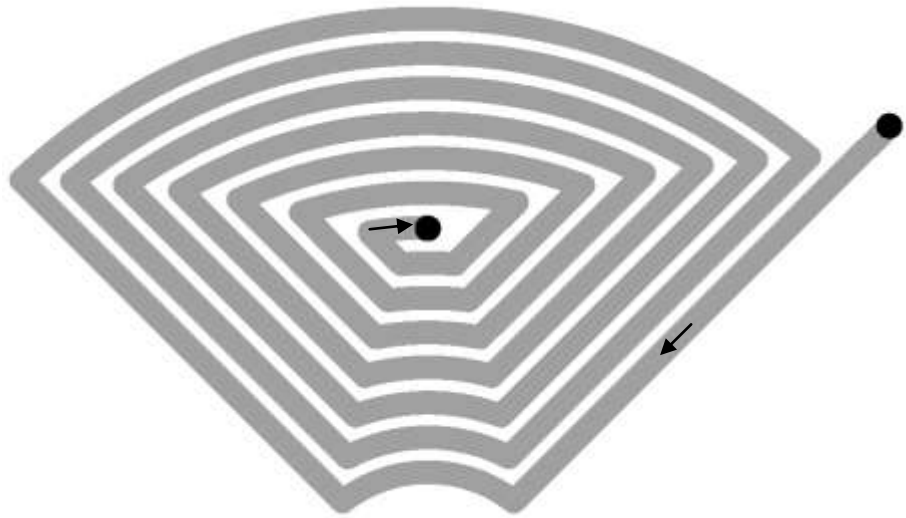
A track plotting procedure has been developed for the design of coils in printed circuit brushless motors. The procedure maximizes the number of turns in the printed spiral shaped coil for given values of substrate inner radius, substrate outer radius, minimum track thickness and inter-track clearance. Active sections of the tracks may be purely radial, parallel with each other or may be partly radial and partly parallel. Computer programs, that implement the procedure, automatically produce track plots which can be used directly by the printed circuit production process.

By combining the track plotting procedure with the finite element method, a technique has been developed to predict rotational EMF waveforms of printed circuit motors. The technique, which has been validated by experimental results from six different prototype motors, has been used for printed circuit motor design optimization.

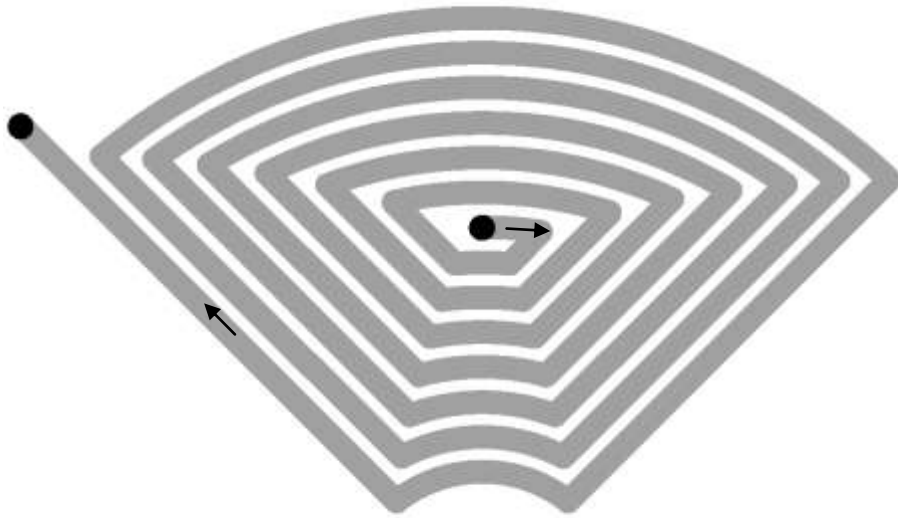
## **References**

- [1] Baudot J H, 'Rotating Electric Machines with Printed Circuit Windings', United States Patent Office, patent number 3144574, Aug 11, 1964.
- [2] Swiggett R L, 'Printed Circuit Armature', United States Patent Office, patent number 2970238, patent number 2970238, patented Jan 31, 1961.
- [3] Tsai M, and Hsu L, 'Design of a Miniature Axial-Flux Spindle Motor with Rhomboidal PCB Winding', IEEE Transactions on Magnetics, Vol 42, No. 10, October 2006, pp 3488-3490.

- [4] Jang G H and Chang J H, 'Development of an Axial-Gap Spindle Motor for Computer Hard Disk Drives Using PCB Winding and Dual Air Gaps', IEEE Transactions on Magnetics, vol 38, No. 5, September 2002, pp 3297-3299.
- [5] Low T S, Jabbar M A, and Tan T S ' Design Aspects and Performance of Slotless PM Motor for Hard Disk Drives', Magnetic Technology Centre, National University of Singapore, Singapore
- [6] Hugel J, Amrhein W, Dietrich F, 'Elektronisch Kommutierter Synchronmotorantrieb', European Patent Office, patent number EP0619639A1, 18 December, 1989.



a)



b)

Figure 1: (a) Top Layer Spiral (b) Bottom Layer Spiral

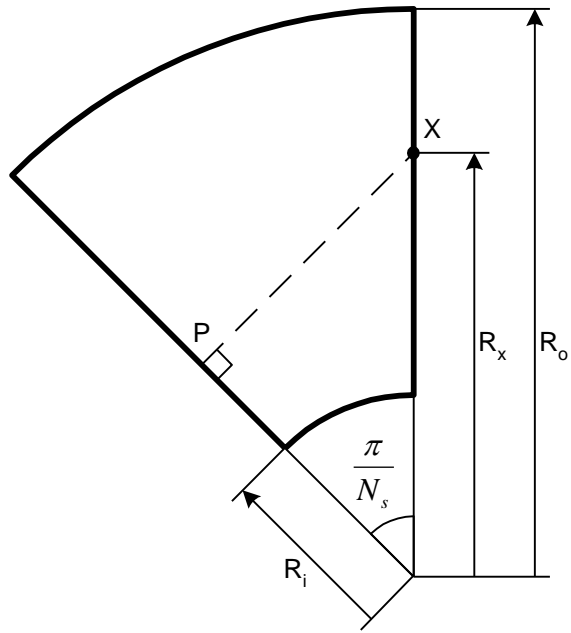


Figure 2: Half Spiral Section of Substrate

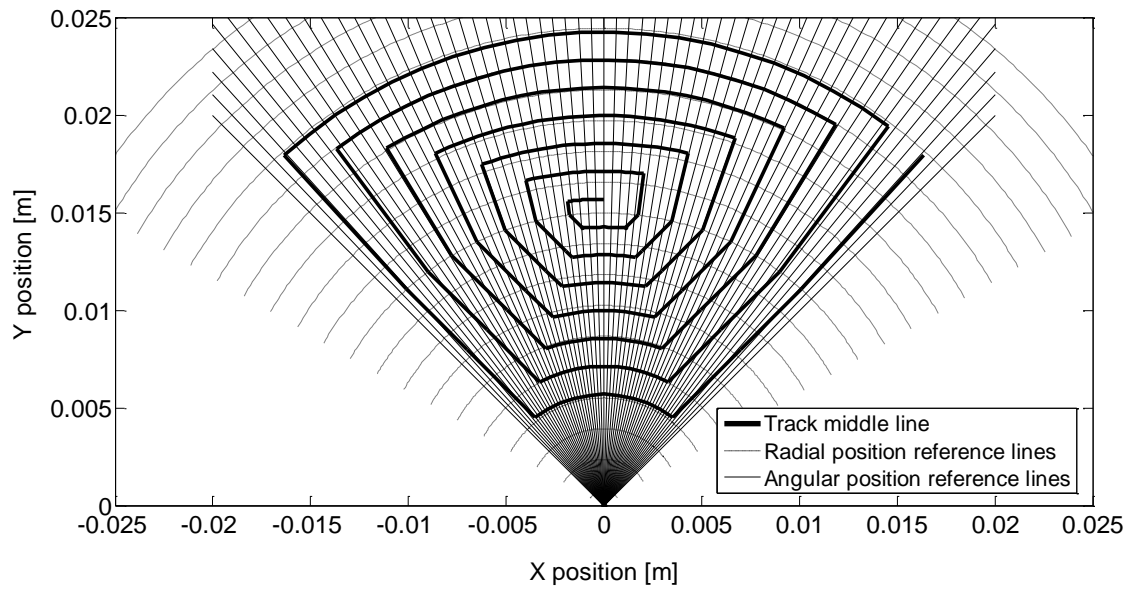


Figure 3: Mixed Track (showing reference lines used for EMF evaluation)

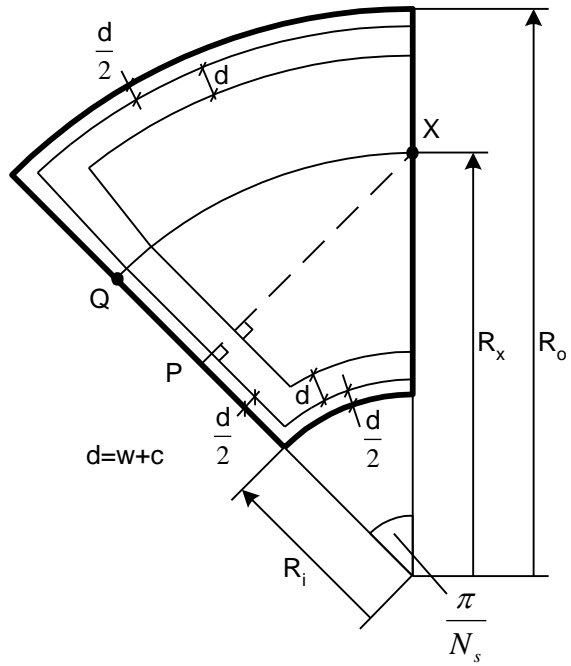


Figure 4: Section of Substrate (Mixed Track Sections)

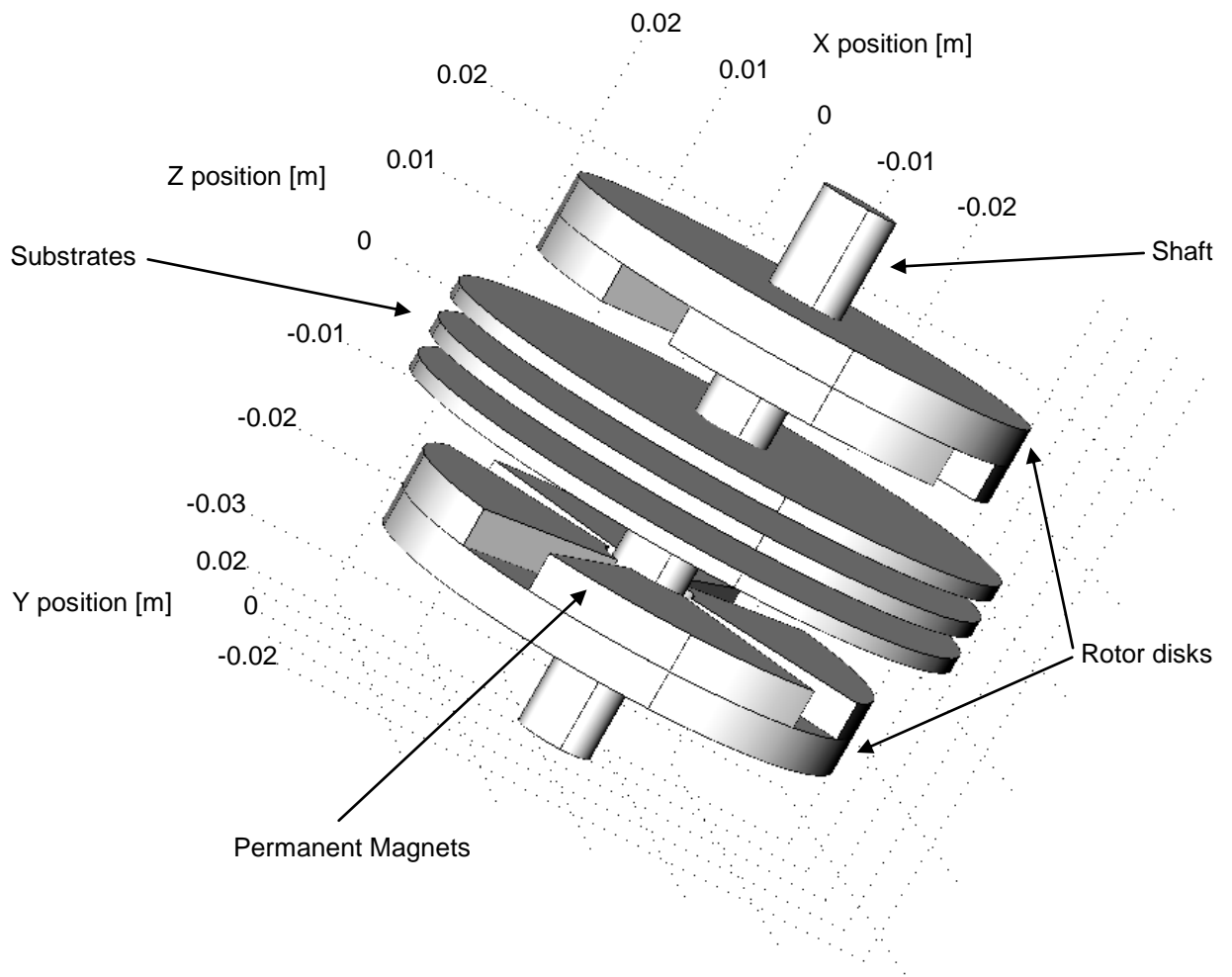


Figure 5: Exploded View of one of six Test Motors

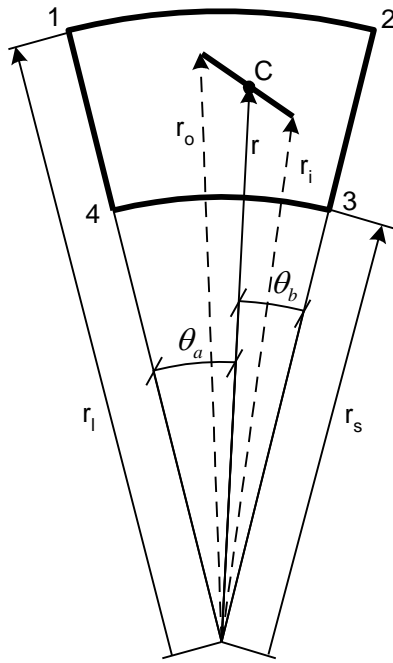


Figure 6: Track Segment in a Cell (segment centred at point C)

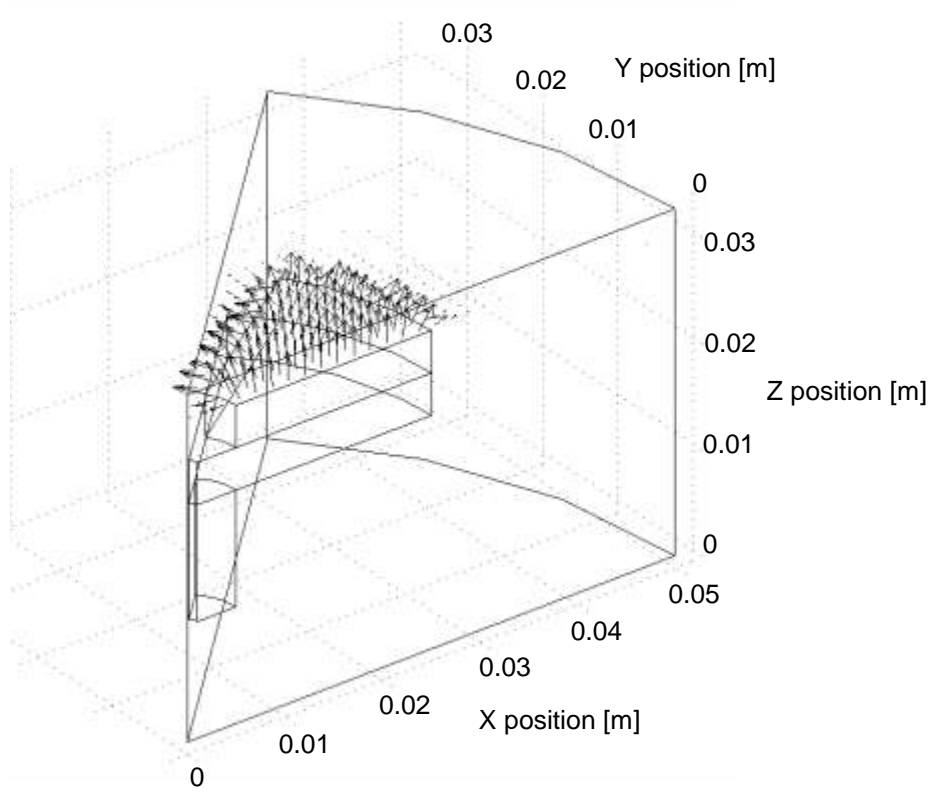


Figure 7: FEMLAB® Model of the Rotor (Half Pole Pitch)

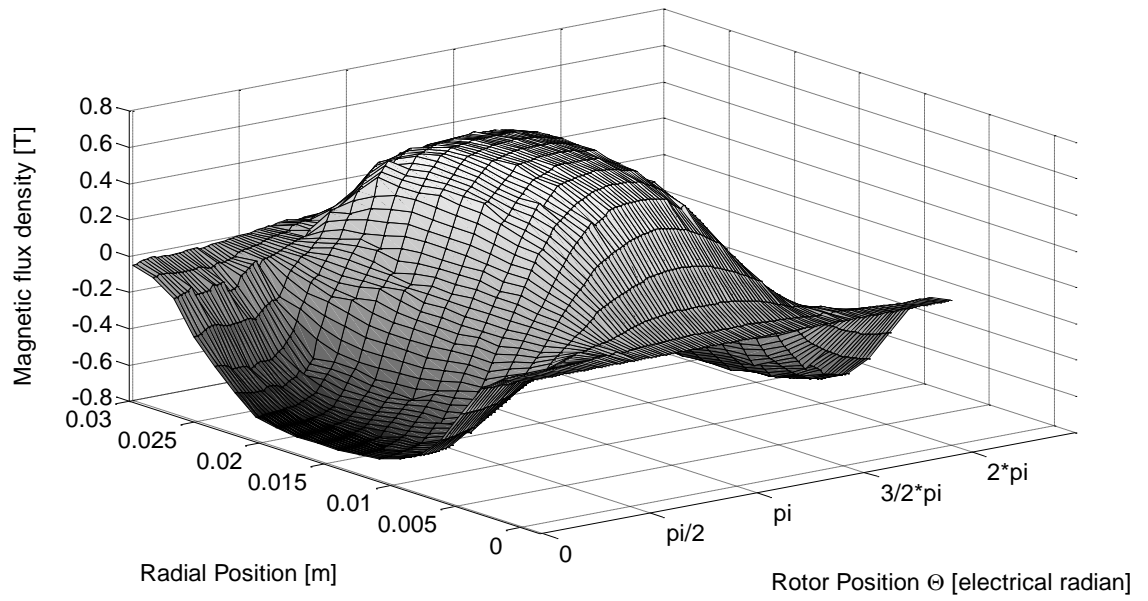


Figure 8: Output from Finite Element Analysis (Axial Flux Density)

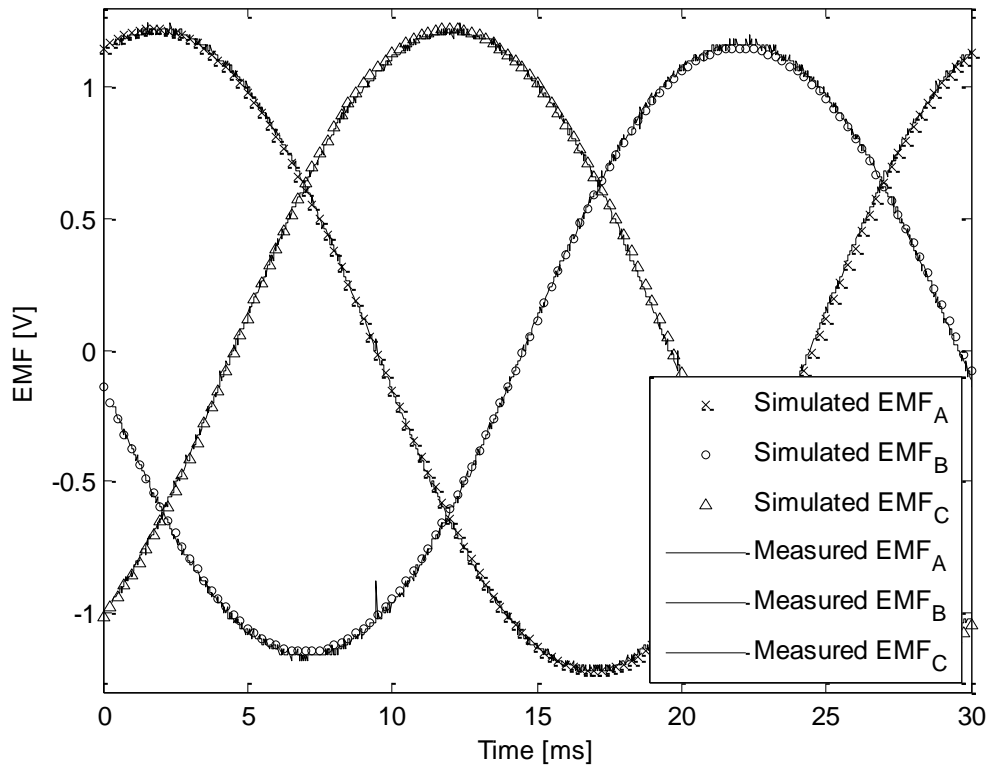


Figure 9: Phase EMF Waveforms (Test Motor No. 1, 1000 r/min)

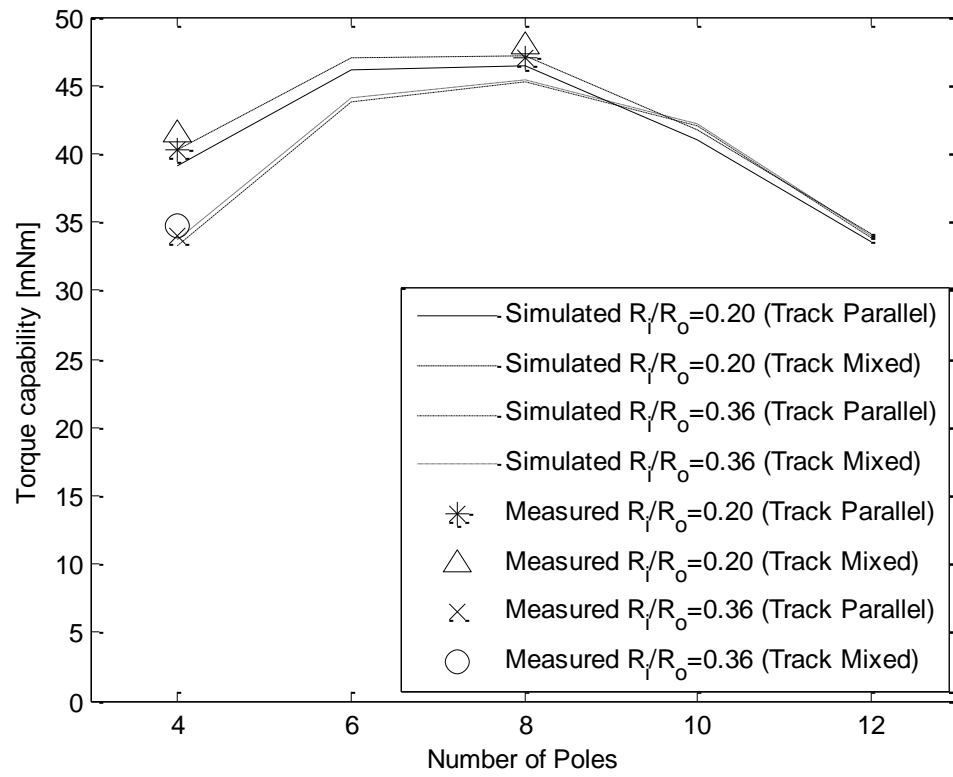


Figure 10: Torque capability versus Number of Poles

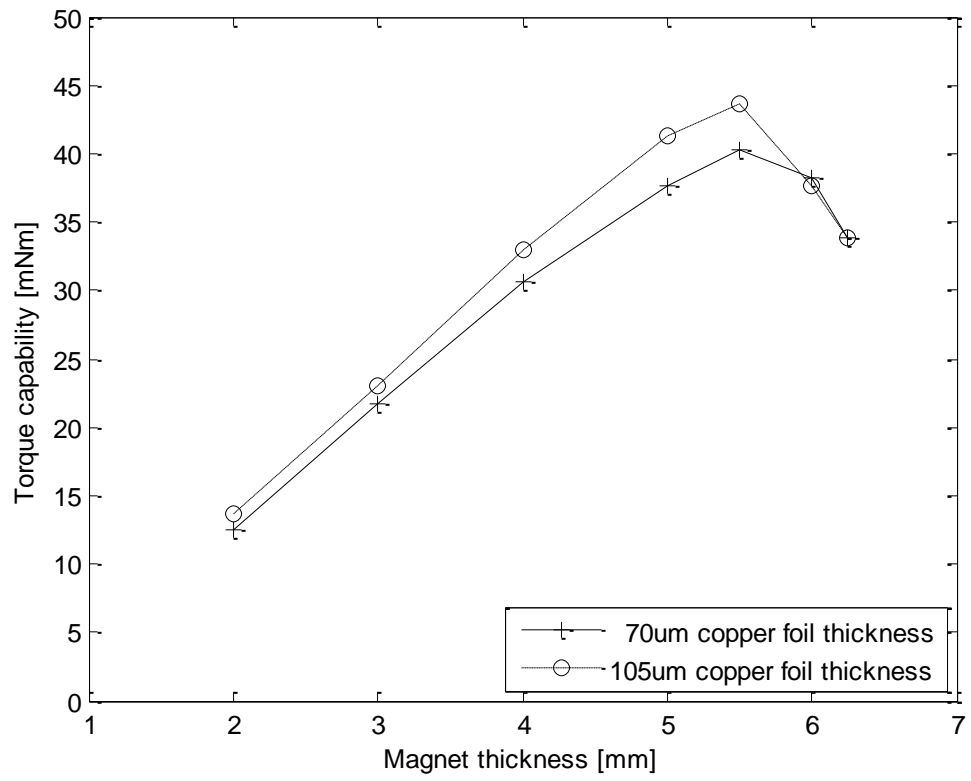


Figure 11: Torque capability versus Magnet thickness

Table 1: Motor Test Data

	$\frac{R_i}{R_o}$	$P$	Track Type	$N$	$B_{g\ peak} [T]$	$E [V_{rms}]$		$R [\Omega]$		$\left(\frac{E}{\omega_m}\right)\sqrt{\frac{P_i}{R}} [mNm]$
						(pred.)	(meas.)	(pred.)	(meas.)	(meas.)
1	0.20	4	Parallel	7	0.708	0.816	0.846	0.092	0.092	40.3
2	0.20	4	Mixed	7	0.708	0.810	0.840	0.085	0.084	42.0
3	0.36	4	Parallel	6	0.702	0.675	0.689	0.087	0.086	34.0
4	0.36	4	Mixed	6	0.702	0.672	0.687	0.084	0.083	34.5
5	0.20	8	Parallel	5	0.655	0.987	1.000	0.093	0.095	47.0
6	0.20	8	Mixed	5	0.655	0.975	0.987	0.090	0.091	47.4

Table 2: Printed Circuit Motor Design Example

<b>Design Parameter</b>	<b>Degree of Flexibility</b>
Outer Radius ( $R_o$ )	$R_o = 25$ mm ( $R_o$ defined in section 1)
Inner Radius ( $R_i$ )	$R_i = 5$ mm
Number of poles (P)	$P = 4$ (Chosen on basis of mechanical requirement and drive switching frequency)
Total thickness ( $t_a$ )	$t_a = 28$ mm
Rotor Iron thickness ( $t_i$ )	$t_i > 1$ mm (for mechanical stability)
Rotor peak flux density ( $B_s$ )	$B_s = 1.4$ T $\pm 0.1$
Stator/Magnet Clearance ( $t_c$ )	0.3 mm
Insulation layer thickness	Foil 1: 100 $\mu$ m ; Foil 2: 100 $\mu$ m
Track thickness	Foil 1: 70 $\mu$ m ; Foil 2: 105 $\mu$ m
Clearance between tracks	Foil 1: 230 $\mu$ m ; Foil 2: 300 $\mu$ m
Minimum track width	Foil 1: 200 $\mu$ m ; Foil 2: 300 $\mu$ m
Maximum track width	Foil 1: 2.5 mm ; Foil 2: 2.5 mm (to avoid stator eddy currents)
Max allowable stator power loss ( $P_1$ )	$P_1 = 2.3$ W
Magnet thickness	$1\text{mm} < t_m < t_{\text{max}}$ ; ( $t_{\text{max}}$ determined by minimum $t_s$ )
Minimum Magnet thickness delta	0.25 mm
Remanence ( $B_r$ )	$B_r = 1.24$ T
EMF (at 1000 rpm)	1V $\pm 10\%$